CHAPTER IV
ANION EXCHANGE AND CATALYTIC PROPERTIES OF A SERIES OF Cu(II)-4,4'-BPY-CARBOXYLATO FRAMEWORKS

4.1 Introduction

The design and synthesis of extended frameworks via supramolecular interactions represents a new area of considerable interest.[94,95] In particular, hydrogen bonding has been exploited for molecular recognition associated with biological activity, and for engineering of molecular solids. [94,95] Much progress has been made in the construction of organic building blocks into 1D, 2D and 3D hydrogen-bonding architectures,[96] and the use of metal complexes as building blocks to assemble multi-dimensional frameworks by hydrogen bonding has also attracted much recent attention, and the resulting products are often expected to exhibit certain desirable electronic, magnetic, or inclusion behavior.[97] In this regard, the formation of such frameworks is highly influenced by several factors such as the coordination nature of the metal ions, the structural characteristics of the polydentate ligands, counterions, and so on.[98] In some cases, a subtle alteration in any of these factors can lead to the formation of new framework architectures.

Ions and small molecules, when being incorporated as guest species in coordination compounds, do not only have a major influence on the construction of the networks and may lead to novel geometries,[99] but the new host–guest materials may also play an important role in materials science, for example, in roles such as chemical sensors and ion exchange materials.[60] Kitagawa et al., for example, successfully constructed a series of porous Cu(II)/**4,4′-bpy** coordination polymers via addition of different anions[77] In coordination networks in general the **4,4′-bpy** ligands may act as bidentate bridging, or as monodentate terminal modes, resulting in 1D linear, zig zag, ladder, molecular antenna railroads and chains, 2D bilayer, square and rectangular grid networks, or 3D non-interpenetrating and interpenetrating networks.

On the basis of these studies in a series of porous Cu(II)-**4,4'-bpy**-carboxylato coordination polymers using different monocarboxylate regulators, nine new

compounds have been successfully constructed via addition of different anions. The selection of the organic and anionic components has been investigated for construction of compounds intriguing structural motifs and potentially useful properties. In this chapter, the structures of two porous coordination polymers, *i.e.* the two-dimensional layered networks, $\{[Cu_3(\mathbf{4,4'\text{-}bpy})_3(\mu\text{-}OOCH)_4(H_2O)_2](ClO_4)_2(H_2O)_6\}_n$ (**12**) and $\{[Cu_2(\mathbf{4,4'\text{-}bpy})_2(\mu\text{-}OOCCH_3)_3](PF_6)(H_2O)\}_n$ (**18**) are describes in detail and compared with those of the remaining compounds (**12-17, 19** and **20**). The crystals of $\{[Cu_3(\mathbf{4,4'\text{-}bpy})_2(\mu\text{-}OOCH)_4(H_2O)_2](X)_2(H_2O)_6\}_n$ when $X = PF_6^-$ (**13**), $CF_3SO_3^-$ (**15**), and $\{[Cu_2(\mathbf{4,4'\text{-}bpy})_2(\mu\text{-}OOCCH_3)_3](X)(H_2O)\}_n$ when $X = ClO_4^-$ (**17**), BF_4^- (**19**), $CF_3SO_3^-$ (**20**) appeared not good enough for X-ray structure analysis, thus the structures of these compounds have been proposed only by elemental microanalyses, spectroscopic properties (IR, EPR and reflectance spectra) and their XRPD patterns. The structural data of compounds **14** and **16** are given in the supplementary data. The thermal and optical properties, dynamic structural transformation by removal and reintroduction of guest molecules, anion-exchange and catalytic reactivity of all frameworks in a series of copper(II)-**4,4'-bpy**-carboxylato compounds are investigated.

4.2 Crystal structures of $\{[Cu_3(4,4'\text{-bpy})_3(\mu\text{-OOCH})_4(H_2O)_2](ClO_4)_2(H_2O)_6\}_n$ (12) and $\{[Cu_2(4,4'\text{-bpy})_2(\mu\text{-OOCCH}_3)_3](PF_6)(H_2O)\}_n$ (18)

4.2.1 Crystal Structure Determination

Measurements on single crystals of **12** and **18** were performed with a Nonius Kappa CCD diffractometer with graphite-monochromated Mo Kα radiation (λ = 0.71073 Å). DENZO-SMN was used for data integration and SCALEPACK corrected data for Lorentz-polarization effects.[100] The structures of both compounds were solved by direct methods with the package SIR92,[101] and the refinement and all further calculations were carried out using the SHELX-TL suite.[102] All non-hydrogen atoms were refined anisotropically. The H atoms were introduced at calculated positions and refined with a fixed geometry with respect to their carrier atoms. The crystal and refinement details of both compounds are listed in Table 4.1, selected bond lengths and angles are given in Tables 4.2 and 4.3, respectively. The crystal and

refinement details of the remaining compounds (**14** and **16**) are given in supplementary data (on CD-ROM inside the back cover of this thesis).

Table 4.1 Crystal and refinement data for compounds **12** and **18**

Compound	**12**	**18**
Empirical formula	$C_{34}H_{44}Cl_2Cu_3N_6O_{24}$	$C_{26}H_{27}Cu_2F_6N_4O_7P$
Formula weight	1182.27	779.57
T (K)	173(2)	173(2)
Crystal system	Monoclinic	Monoclinic
Space group	*P2/c*	*P21/c*
a (Å)	12.294(2)	11.708
b (Å)	11.071(2)	15.839
c (Å)	16.729(3)	18.196
α (°)	90.00	90.00
β (°)	91.09(3)	117.34
γ (°)	90.00	90.00
V (Å^3)	2276.5(7)	2997.4
Z	2	4
D_{cal} (g cm^{-3})	1.725	1.727
μ (mm^{-1})	1.600	1.561
F(000)	1206	1576
θ range (°)	3.05-27.59	2.19 - 27.58
GOF	1.016	0.995
Final R indices	$R1$ = 0.0609	$R1$ = 0.0596
[I>2σ(I)]	$wR2$ = 0.1309	$wR2$ = 0.1442
R indices (all data)	$R1$ = 0.0991	$R1$ = 0.0946
	$wR2$ = 0.1485	$wR2$ = 0.1678
Largest difference peak and hole (e Å^{-3})	0.941, –1.026	0.716, –0.886

$R = \Sigma||F_o| - |F_c||/\Sigma|F_o|$, $R_w = [\Sigma w\{|F_o| - |F_c|\}^2/\Sigma w|F_o|^2]^{1/2}$.

Table 4.2 Selected bond lengths (Å) and angles (°) for **12**

Bond lengths			
Cu1—O1	1.989(3)	Cu2—O4	2.011(4)
Cu1—O5a	1.990(3)	Cu2—O4b	2.011(4)
Cu1—N11	2.007(4)	Cu2—N31	2.012(5)
Cu1—N21	2.026(4)	Cu2—N41	2.013(5)
Cu1—O5	2.355(3)	Cu2—O3	2.309(3)
Cu1–O3b	2.593(3)	Cu2—O3b	2.309(3)
Bond angles			
O1—Cu1—O5a	178.29(12)	O4—Cu2—O4b	179.9(2)
O1—Cu1—N11	89.67(14)	O4—Cu2—N31	89.94(11)
O5a—Cu1—N11	90.78(14)	O4b—Cu2—N31	89.94(11)
O1—Cu1—N21	87.89(14)	O4—Cu2—N41	90.06(11)
O5a—Cu1—N21	91.78(14)	O4b—Cu2—N41	90.06(11)
N11—Cu1—N21	175.56(15)	N31—Cu2—N41	180.000
O1—Cu1—O5	100.53(12)	O4—Cu2—O3	92.16(14)
O5a—Cu1—O5	77.80(13)	O4b—Cu2—O3	87.85(14)
N11—Cu1—O5	91.36(12)	N31—Cu2—O3	95.09(8)
N21—Cu1—O5	92.72(13)	N41—Cu2—O3	84.91(8)
O1– Cu1– O3b	55.41(12)	O4—Cu2—O3b	87.85(14)
		O4b—Cu2—O3b	92.16(14)
		N31—Cu2—O3b	95.09(8)
		N41—Cu2—O3b	84.91(8)
		O3—Cu2—O3b	169.82(17)

Symmetry operations: (a) 1-x, y, 0.5-z; (b) -x, y, 0.5-z; (c) x, -1+y, z; (d) x, 1+y, z; (e) -x, 1+y, 0.5-z

Table 4.3 Selected bond lengths (Å) and angles (°) for **18**

Bond lengths			
Cu1—O3a	1.962(3)	Cu2—O7	1.972(3)
Cu1—N31	2.008(3)	Cu2—O9b	1.984(3)
Cu1—N21	2.015(3)	Cu2—N11c	2.006(3)
Cu1—O5	2.060(3)	Cu2—N41d	2.008(3)
Cu1—O1	2.175(3)	Cu2—O9	2.366(3)
Cu1—O7	2.895(3)	Cu2—O12	2.739(3)
Bond angles			
O3a—Cu1—N31	91.38(14)	O7—Cu2—O9b	175.41(13)
O3a—Cu1—N21	92.11(14)	O7—Cu2—N11c	87.30(12)
N31—Cu1—N21	175.08(15)	O9b—Cu2—N11c	92.99(12)
O3a—Cu1—O5	144.60(12)	O7—Cu2—N41d	87.39(12)
N31—Cu1—O5	90.94(14)	O9b—Cu2—N41d	92.34(12)
N21—Cu1—O5	88.21(13)	N11c—Cu2—N41d	174.67(13)
O3a—Cu1—O1	125.72(14)	O7—Cu2—O9	105.39(12)
N31—Cu1—O1	88.30(14)	O9b—Cu2—O9	79.19(12)
N21—Cu1—O1	86.85(14)	N11c—Cu2—O9	90.08(13)
O5—Cu1—O1	89.65(14)	N41d—Cu2—O9	90.81(13)

Symmetry operations: (a) 1-x, -y, -z; (b) 1-x, 1-y, -z; (c) -1+x, 0.5-y, -0.5+z; (d) 1+x, 0.5-y, 0.5+z

4.2.2 Structure Description

Crystal structure of $\{[Cu_3(4,4'\text{-bpy})_3(\mu\text{-OOCH})_4(H_2O)_2](ClO_4)_2(H_2O)_6\}_n$ (12)

The 2D structure of compound **12** exhibits two different types of copper(II) ions each with elongated octahedral N_2O_4 coordination environments (Figure 4.1).

Cu1 is characterized by an elongated octahedral coordination environment, owing to the small bite angle of one formato ligand with the μ-O,O',O' bridging mode (the angle O3b–Cu1–O1 is only 55.41(12)°; Table 4.2). The basal plane is constituted of two oxygen atoms belonging to one μ-O,O',O'-formato ligand (O1) and one monoatomic bridged μ-O,O formato ligands (O5a) and two **4,4'-bpy** nitrogen atoms (N11 and N21). The octahedron is completed by two oxygen atoms belonging to one μ-O,O',O'-formato ligand (O3b) and one monoatomic bridged μ-O,O formato ligands (O5) at the axial positions with the Cu-O distances of 2.593(3) and 2.355(3) Å, respectively. The Cu–O and Cu–N bond distances[103] can be considered as normal for this type of CuN_2O_4 coordination environment (Table 4.2).

Cu1 is located at an inversion center and is bridged to symmetry-related Cu1A ions via two monoatomic bridged μ-O,O'-formato ligands (O5 and O5a) and Cu2 ions via one μ-O,O',O'-formato ligand, generating a linear trinuclear [Cu1A, Cu1, Cu2] cluster, linking a polymeric chain (red oxygens in the formate ligands in Figures 4.1 and 4.2).

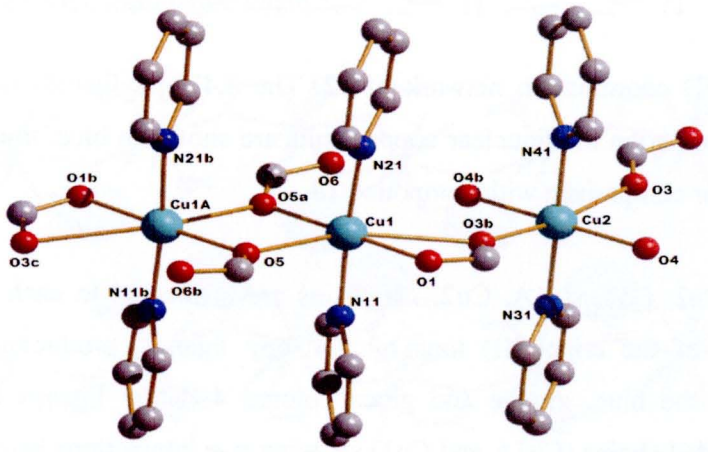

Figure 4.1 Representation of the linear trinuclear unit of **12** showing the atom labeling scheme for the copper(II) environments. The perchlorate anions, the lattice water molecules and the H atoms are not shown for clarity.

The coordination environment around the Cu2 ion is an almost perfect (elongated) octahedron based on the basal angles, varying from 89.94(11) to 90.06(11)°, are close to the ideal value of 90°. At the basal plane, Cu2 is coordinated by two water molecules (O4 and O4b) and two nitrogen atoms (N31 and N41) belonging to two **4,4'-bpy** ligands. The axial positions are occupied by two oxygen atoms (O3 and O3b) from different μ-O,O',O'-formato ligands at common distances (Cu2-O distances = 2.309 Å).

Cu2 is bridged to Cu1 and Cu1A ions via two μ-O,O',O'-formato ligands, generating a linear trinuclear [Cu1, Cu2, Cu1A] cluster, linking a polymeric chain exhibiting the sequence {Cu2, Cu1, Cu1A, Cu2,...} (see red oxygen atoms in the formate ligands in Figure 4.2).

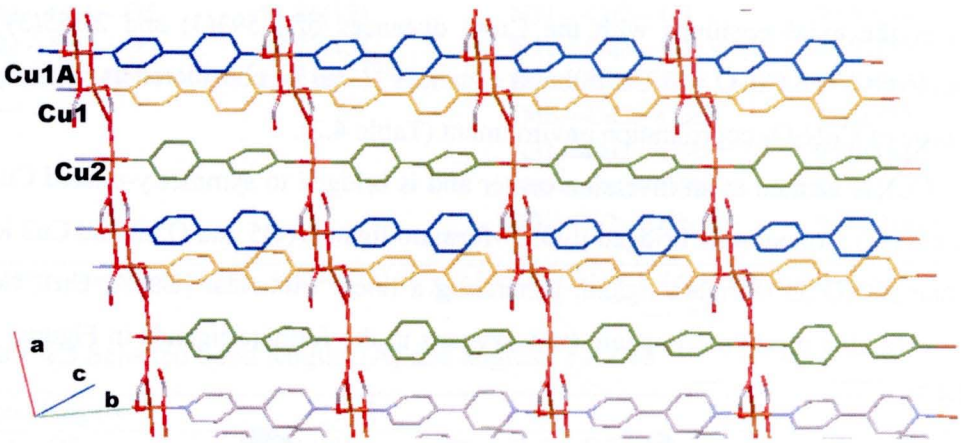

Figure 4.2 2D coordination network of **12**. The **4,4'-bpy** ligands involved in the formation of trinuclear copper units are shown in blue, orange and green for comparison with compound **18**.

The {Cu2, Cu1, Cu1A, Cu2,...} chains are connected to each other through coordination of the copper(II) ions by **4,4'-bpy** ligands, producing a 2D layer, indicated by the blue, orange and green colored **4,4'-bpy** ligands in Figure 4.2. Double-stranded chains (Cu1A and Cu1) showing π–π interactions between two **4,4'-bpy** units (with centroid-to-centroid distances ranging from 3.467(4) to 3.682(4) Å, see blue and orange colored **4,4'-bpy** ligands in Figure 4.2) are connected to each other via a different infinite single chain (see green **4,4'-bpy** ligands in Figure 4.2).

This spatial arrangement produces a triple-stranded coordination chain (Figures 4.1 and 4.3). However, the 2D layers are closely packed, which allows the coordination of a small molecule, namely two water molecules (O4 and O4b in Figures 4.3 and 4.4) at Cu2 center. These coordinated water molecules are hydrogen-bonded to lattice water molecules (O4···O6Wb = 2.745(4) Å and O4···O9Wa = 2.663(4) Å). The fascinating crystal packing of the solid-state structure of **12** is shown in Figure 4.5. As anticipated, the two π-acidic rings are involved in anion–π interactions.[104] Indeed, each perchlorate ion exhibits intermolecular anion–π interactions with two **4,4'-bpy** rings

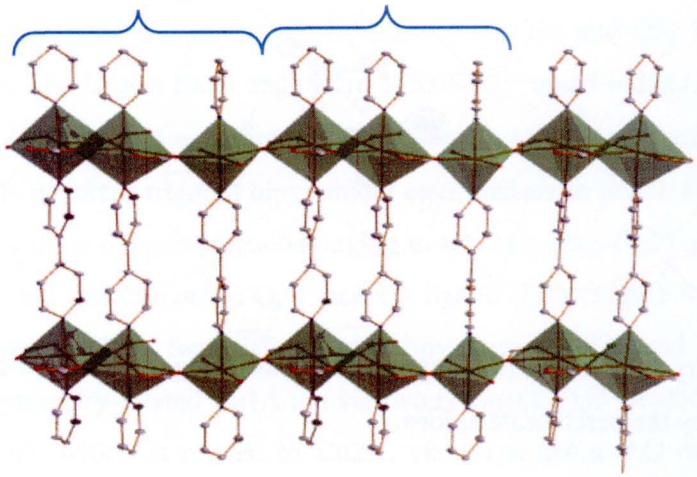

Figure 4.3 2D coordination network of **12**. This spatial arrangement produces a triple-stranded coordination chain.

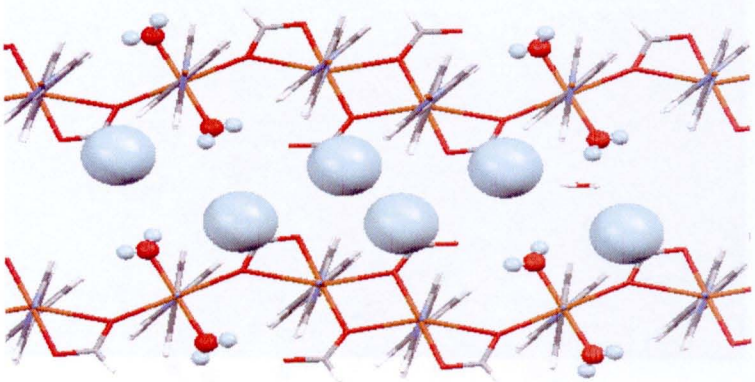

Figure 4.4 Illustration of the non-steric effect from the formato hydrogen groups (shown in the space-filling mode) in **12**, which allows the coordination of two water molecules (O4 and O4b).

from an adjacent (Figure 4.5). Furthermore, the ClO_4^- anions occupy the voids in the crystal lattice and apparently do play a significant role in the formation of the framework (especially because their interactions with the **4,4'-bpy** ligands with adjacent layers; the $O(ClO_4^-)\cdots C$ contact distances are in the range 4.267(12)-4.539(12) Å) leading to the formation of the three-dimensional structure (Figure 4.6).

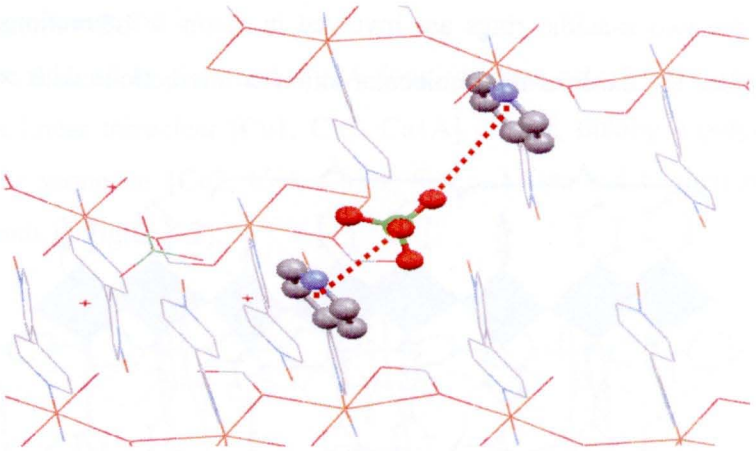

Figure 4.5 Crystal packing of compound **12** illustrating the anion–π contacts shown by the perchlorate anions.

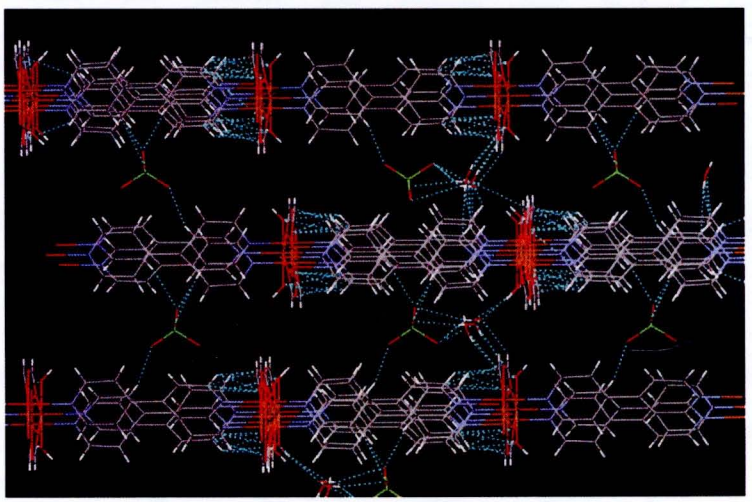

Figure 4.6 Packing diagram with hydrogen bond (dash-lines), showing the three-dimensional structure of **12.**

Crystal structure of $\{[Cu_2(4,4'\text{-bpy})_2(\mu\text{-}OOCCH_3)_3](PF_6)(H_2O)\}_n$ (18)

The simple replacement of formate by acetate during the synthetic procedure (used to prepare **12**) produces significant structural changes in the crystal lattice of the resulting coordination compound $\{[Cu_2(\mathbf{4,4'\text{-}bpy})_2(\mu\text{-}OOCCH_3)_3](PF_6)(H_2O)\}_n$ (**18**). As is shown in Figure 4.7, compound **18** also contains two types of copper(II) ions, intermediate five-coordinate (Cu1) and compressed octahedral (Cu2) geometries.

Cu1 lies at an inversion center and exhibits a five-coordinate environment, intermediate between trigonal bipyramid and square pyramid. The five-coordinate CuN_2O_3 chromophore is constituted of two nitrogen atoms (N31 and N41) belonging to two **4,4'-bpy** ligands and three oxygen atoms (O1, O3a and O5) from different acetato ligands. The largest basal angles are 175.08(15)° and 144.60(12)°, hence the geometry may be described as an intermediate five-coordinate geometry ($\tau = 0.51$), slightly towards distorted trigonal bipyramidal environment in which the basal plane is constituted of three oxygen atoms belonging to two *syn,syn*,μ-O,O'-acetato ligands (O1 and O3a) and one *syn,anti*,μ-O,O'-acetato ligand (O5) (Figure 4.7). The axial positions are occupied by two different **4,4'-bpy** ligands (N21 and N31). Cu1 is connected to symmetry-related Cu1A ion via two *syn,syn*,μ-O,O'-acetato ligands, and is linked to Cu2, which is related to Cu2A, via a *syn,anti*,μ-O,O'-acetato ligand, generating a polymeric chain exhibiting the sequence {Cu1A, Cu1, Cu2, Cu2A...} (see red colored oxygen atoms of the acetate ligands in Figure 4.8). The Cu–O and Cu–N bond distances[105] can be considered as normal for this type of CuN_2O_3 coordination environment (Table 4.7).

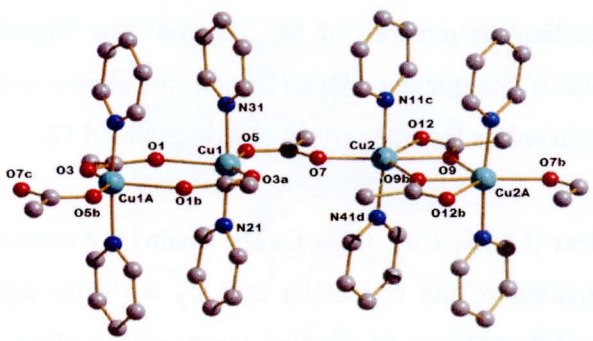

Figure 4.7 Representation of the tetranuclear unit of **18** showing the atom labeling scheme for the copper(II) ions. The hexafluoridophosphate anions, the lattice water molecules and the H atoms are not shown for clarity.

Cu2 also lies at an inversion center and is coordinated at the basal plane of the compressed octahedron by four oxygen atoms from three acetato ligands (O7, O12, O9 and O9b). Cu2 is symmetry related to Cu2A via two ,μ-O,O',O'-acetato ligands and is linked to Cu Cu1A which is symmetry related to Cu1, generating a linear tetranuclear [Cu2, Cu2A, Cu1A, Cu1] cluster, linking a polymeric chain (red colored acetate ligands in Figure 4.8). The axial positions are occupied by two **4,4'-bpy** ligands (N11c and N41d), linking Cu2 to symmetry-related Cu1 ion, generating a polymeric chain exhibiting the sequence {Cu2, Cu1, Cu2, Cu1...} (green and purple colored **4,4'-bpy** ligands in Figures 4.8 and 4.9). The Cu–O and Cu–N bond distances are in normal ranges for this type of coordination moiety. The basal angles varying from 59.38(12) to 105.39(12)° (Table 4.3) are indicative of a strong distortion of the octahedron, attributed to the small bite angle of the μ-O,O'-acetato ligand (O12–Cu2–O9 = 59.38(12)°) and very long Cu-O basal distances of 2.739(3) and 2.366(3) Å.

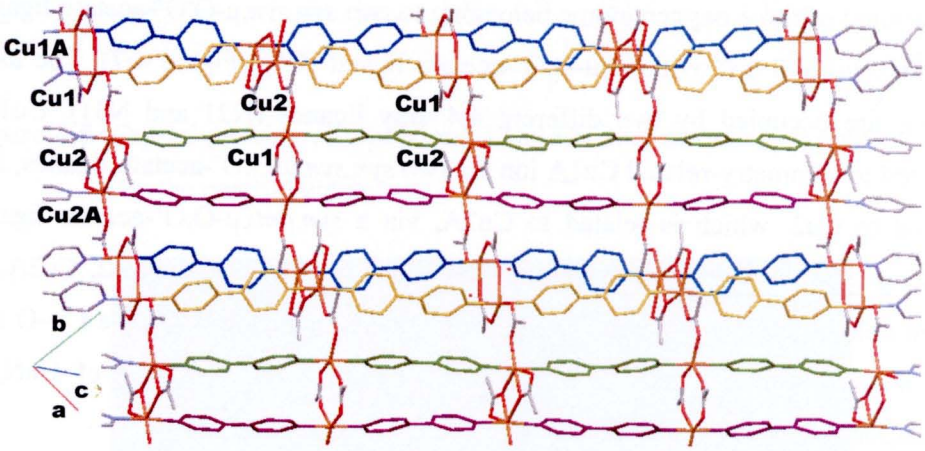

Figure 4.8 2D coordination network of **18**. The **4,4'-bpy** ligands involved in the formation of tetranuclear copper(II) units are shown in blue, orange, green and purple colors for comparison with compound **12**.

The tetranuclear [Cu1A, Cu1, Cu2, Cu2A] chains are connected to each other through the coordination of the copper(II) ions by **4,4'-bpy** ligands, producing a quadruple-stranded chain 2D layer exhibiting the sequence {Cu1, Cu2, Cu1,...} for the intermediate five-coordinate environment and {Cu2, Cu1, Cu2,...} for the octahedral environment (Figures 4.8 and 4.9). This arrangement gives rise to two double-stranded chains, illustrated by the blue and orange marks for Cu1 and Cu1A,

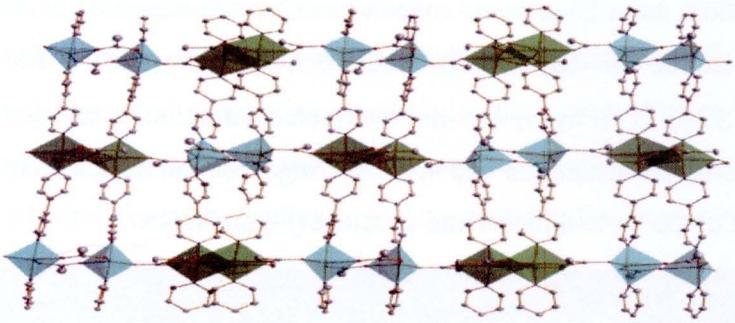

Figure 4.9 2D coordination network of **18**. This spatial arrangement produces a quadruple-stranded coordination chain alternating the intermediate five-coordinate and octahedral geometries in each chain.

and green and purple marks for Cu2 and Cu2A in Figure 4.8, alternating between an intermediate five-coordinate environment and an octahedral one (Figure 4.9). These coordination polymeric chains are closely related to those observed for compound **12** (see Figure 4.3). In contrast to the hydrogen groups of the formato ligands in **12**, the methyl groups of the acetato ligands in **18** do not allow a close packing of triple-stranded polymeric chains (see Figures 4.3 and 4.4), as the result of steric constraints. Consequently, the tetranuclear copper(II) units in **18** are more separated from each other than those in **12** (Figure 4.10). Indeed, the shortest intermolecular Cu···Cu separation distance is 9.544(12) Å for compound **18**, while the shortest intermolecular Cu···Cu distance is 7.855(11) Å for **12,** and which only allows the coordination of two water molecules (O4 and O4b in Figures 4.1 and 4.4).

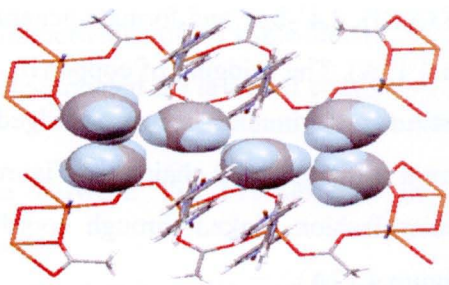

Figure 4.10 Illustration of the steric bulk in **18** resulting from the acetate methyl groups (shown in the space-filling mode), preventing the interconnection of the triple-stranded chains and not allowing the coordination of water molecules.

In addition, these large voids contain hexafluoridophosphate anions, which are hydrogen bonded to **4,4'-bpy** ligands in adjacent layers (F1···C26 = 3.169(12) Å and F6···C13 = 3.126(15) Å, as well as the intermolecular anion–π interactions between each hexafluoridophosphate ion and **4,4'-bpy** rings from an adjacent layer leading to the formation of the three-dimensional structure (Figure 4.11).

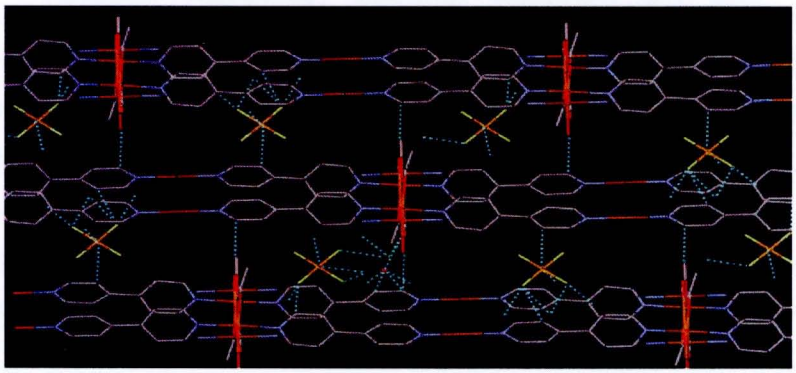

Figure 4.11 Packing diagram with hydrogen bond and anion-pi contacts (dash-lines), as seen from the three-dimensional structure of **18**.

4.2.3 Effect of Carboxylate-regulator on Topologyies of 12 and 18

The steric effect on the architecture has been investigated by using a slightly different monocarboxylato namely formato and acetato moieties as secondary co-ligands of [Cu(II)/**4,4'-bpy**] coordination units, while applying the same reaction conditions. The structures lead to the formation of different structural motifs (Figure 4.12).

The combination of Cu(II), **4,4'-bpy** and formate generates a triple-stranded 2D framework for **12** (Figure 4.12A). The bridging of copper(II) ions by formato ligands produces a 1D chain constituted of trinuclear formato-bridged units that are linked to two adjacent ones, to form a triple-stranded chain (see Figure 4.2). These chains are arranged in a perpendicular fashion, linked through coordinated 4,4'-bipyridines, resulting in a 2D layer (Figure 4.12A).

Replacing formate with acetate, the structure packing and environment were transformed to generate the 2D network for **18** constituting of tetranuclear acetato-bridged units that are linked to two adjacent ones, to form quadruple-stranded layers (Figures 4.8 and 4.12B). The use of acetate co-ligand yields a 2D network which

presents different structural motifs with that of **12**. Actually, the framework of **18** exhibits two different types of copper(II) ion with the intermediate five-coordinate and compressed octahedral geometries alternating in each chain (Figure 4.9), whereas the framework **12** shows two independent copper(II) chromophores, each with elongated octahedral geometry leading to the connection of each elongated distance along each chain (Figure 4.3).

Indeed, structures of **12** and **18** exhibit trinuclear and tetranuclear carboxylato-bridged moieties, respectively, as secondary building units. Moreover, infinite $\{-Cu-(\mathbf{4,4'\text{-}bpy})-\}_n$ chains are observed for both compounds (see the blue, orange, green and purple colored $\{-Cu-(\mathbf{4,4'\text{-}bpy})-\}_n$ chains in Figures 4.2 and 4.8). Finally, one should note that the copper(II) ions of both compounds have different coordination environments, regardless of the carboxylato co-ligand used. Therefore, the structural diversity and structural motifs of the frameworks obviously originates from the influence of carboxylate-regulator on the topologies of **12** and **18**.

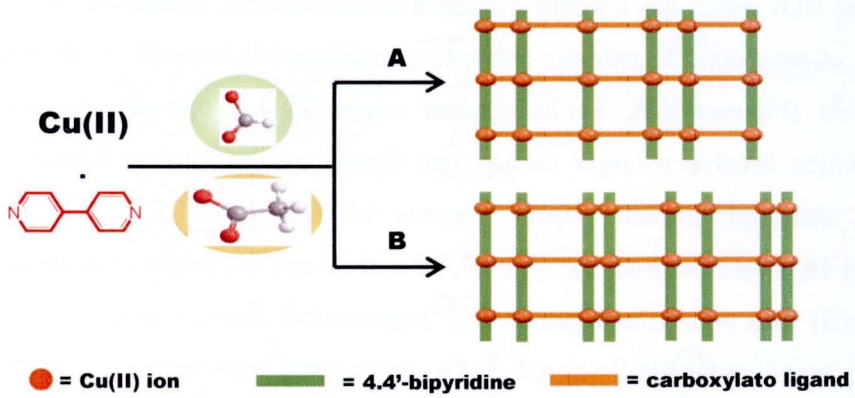

Figure 4.12 Coordination networks of A) triple-stranded 2D layers of compound **12**, B) quadruple-stranded 2D layers of compound **18**.

4.2.4 Comparison between the Frameworks of 12 and 18 and Other Related Compounds

Among nine copper(II)-**4,4'-bpy**-carboxylato compounds obtained in this study (see Table 4.4), four compounds $\{[Cu_3(\mathbf{4,4'\text{-}bpy})_2(\mu\text{-}OOCH)_4(H_2O)_2](X)_2(H_2O)_6\}_n$ when X = ClO_4^- (**12**) and BF_4^- (**14**), $\{[Cu(\mathbf{4,4'\text{-}bpy})(\mu\text{-}OOCH)(NO_3)]\}_n$ (**16**) and $\{[Cu_2(\mathbf{4,4'\text{-}bpy})_2(\mu\text{-}OOCCH_3)_3](PF_6)(H_2O)\}_n$ (**18**) have been crystallographically

characterized. While the crystals of remaining compounds $\{[Cu_3(\mathbf{4,4'\text{-}bpy})_2(\mu\text{-}OOCH)_4(H_2O)_2](X)_2(H_2O)_6\}_n$ when X = PF_6^- (**13**), $CF_3SO_3^-$ (**15**), and $\{[Cu_2(\mathbf{4,4'\text{-}bpy})_2(\mu\text{-}OOCCH_3)_3](X)(H_2O)\}_n$ when X = ClO_4^- (**17**), BF_4^- (**19**), $CF_3SO_3^-$ (**20**) appeared unsuitable for X-ray structure analysis, thus the structures of these complexes have been proposed by elemental microanalyses, spectroscopic properties and XRPD pattern. Compounds **12** and **18** are structurally compared with other relevant coordination polymers and are presented in Table 4.4.

The 2D structure of compounds **12** is isostructural with those of **13, 14** and **15** which all exhibit two independent copper(II) chromophores, each consisting of an elongated octahedral N_2O_4 coordination environment (Figures 4.1 and 4.13). The different guests are located in the cavities, i.e. ClO_4^- (**12**), PF_6^- (**13**), BF_4^- (**14**) and $CF_3SO_3^-$ (**15**). Replacing ClO_4^- with stronger coordinating NO_3^- anions, these anions are indeed coordinated to copper(II) centers and the 2D triple-stranded layers have been transformed to zig-zag 2D layers for **16** (Figure 4.13), indicating that the property of NO_3^- anion has a major influence on the network formation. The zig-zag 2D layers of compound **16** exhibits only one type copper(II) ion with octahedral N_2O_4 environment (Figure 4.13). Similarly, four copper(II)-**4,4'-bpy**-actato compounds (**18-20**) which involve a larger carboxylate ligand exhibit similar topologies, 2D networks, quadruple-stranded layers (Figures 4.8 and 4.9). The 2D structure of compound **18** is also isostructural with **17**, **19** and **20** and exhibits two different types of copper(II) ions with mixed geometries, intermediate five-coordinate based N_2O_3 and compressed octahedrally-based N_2O_4 geometries, alternating in each chain (Figure 4.9). The different guests are filled in the channels for ClO_4^- (**17**), PF_6^- (**18**), BF_4^- (**19**) and $CF_3SO_3^-$ (**20**). This demonstrates that the four anions have no major influence on the network formation. In this study, the feature of the quadruple-stranded 2D networks is very comparable to the triple-stranded 2D networks. Double-stranded ladders in chain structures are linked to one copper(II) chain, forming triple-stranded chains for **12** and **14** (Figures 4.2 and 4.13), while quadruple-stranded 2D networks for **17-20** consist of two double-stranded chains (Figure 4.9) with different copper(II) environments. Therefore, the structural diversity of the frameworks obviously originates from different steric constraints induced by the used carboxylato ligands.

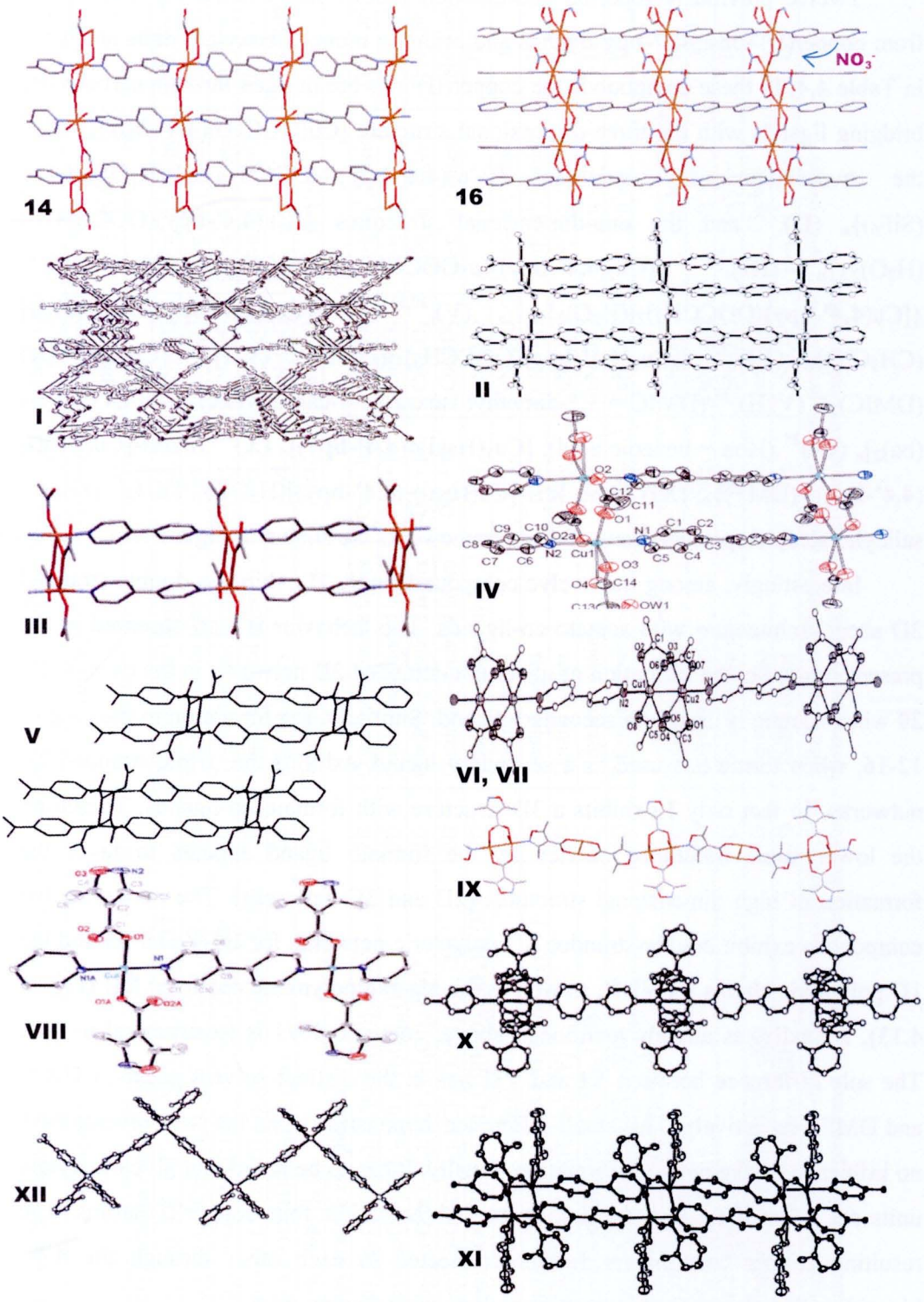

Figure 4.13 Representations of the related structure of some [Cu(II)/**4,4'-bpy**/ carboxylato]-based coordination networks.

Twelve previously reported coordination frameworks exclusively constructed from copper(II) ions, **4,4'-bpy** ligands and bridging monocarboxylato units are listed in Table 4.4. In these compounds the copper(II) ions are bridged through carboxylate bridging ligands with the three-dimensional structure $[Cu(OOCH)_2(\mathbf{4,4'\text{-}bpy})]_n$ (**I**),[26] the two-dimensional structures $\{[Cu_2(\mathbf{4,4'\text{-}bpy})(OOCCH_3)(OH)(H_2O)](H_2O)_2(SiF_6)\}_n$ (**II**),[27] and the one-dimensional structures $\{[Cu(\mathbf{4,4'\text{-}bpy})(OOCCH_3)_2](H_2O)_{2.5}\}_n$ (**III**),[28] $\{[Cu_2(\mathbf{4,4'\text{-}bpy})_2(\mu\text{-}OOCCH_3)_2(OOCCH_3)_2](H_2O\}_n$ (**IV**),[29] $\{[Cu(\mathbf{4,4'\text{-}bpy})(OOCCH_3)_2](H_2O)_3\}_n$ (**V**),[30,31] $\{[Cu_2(\mathbf{4,4'\text{-}bpy})(OOCCH_3)_4](CH_3CN)\}_n$ (**VI**),[32] $\{[Cu_2(\mathbf{4,4'\text{-}bpy})(OOCCH_3)_4](DMF)\}_n$ (**VII**),[33] $[Cu(\mathbf{4,4'\text{-}bpy})(DMIC)_2]_n$ (**VIII**),[34] (DMIC = 3,5-dimethyl isoxazole-4-carboxylate), $[Cu(4,4'\text{-}bpy)_{0.5}(ba)_2]_n$ (**IX**)[35] (Hba = benzoic acid), $[Cu_2(Hsal)4(\mathbf{4,4'\text{-}bpy})]_n$ (**X**)[36] {*trans*-$[Cu(Hsal)_2(\mathbf{4,4'\text{-}bpy})]$ (DMF)}$_n$, (**XI**)[36] and {*cis*-$[Cu(Hsal)_2(\mathbf{4,4'\text{-}bpy})](H_2O)_2\}_n$ (**XII**)[36] (Hsal = salicylic acid). Representations of these frameworks are shown in Figure 4.13.

Interestingly, among the twelve compounds, only **II** exhibits a double-stranded 2D sheet architecture with acetato co-ligands. This behavior is also observed in the present study, i.e. the formation of quadruple-stranded 2D networks in the case of **17-20** when acetate is used as a secondary ligand. Similarly, the formation in the case of **12-16**, when formate is used as a secondary ligand, exhibits the triple-stranded 2D networks. In fact only **I** exhibits a 3D structure with formato co-ligands. Therefore, the lower steric hindrance exerted by the formato ligand appears to favor the formation of high dimensional structures (2D and 3D networks). The remaining ten compounds exhibit doubly-stranded 1D polymeric networks for **III-V** and **XI** and the 1D polymeric chains for **VI-X**, as well as the zig-zag polymeric chain for **XII** (Figure 4.13). Actually, as already mentioned above, compound **VI** is isostructural to **VII**. The sole difference between **VI** and **VII** lies in the distinct solvent guests, CH_3CN and DMF, respectively. This small difference demonstrates that the two solvents have no influence on the network formation. Finally, it has to be noted that all carboxylato units act as bridging ligands, linking two, three and/or four copper(II) atoms. The resulting copper clusters are further connected to each other through the 4,4'-bipyridine ligands generating the higher-dimension frameworks.

Table 4.4 Structural descriptions for the several [Cu(II)/**4,4'-bpy**/carboxylato]-based coordination networks.

Compound	Type	Topology	Geometry	Chromo phore	Mode of (-OCO-)	Reference
Cu(II)/4,4'-bpy/formato compounds						
$\{[Cu_3(\mathbf{4,4'\text{-}bpy})_3(\mu\text{-}OOCH)_4(H_2O)_2](ClO_4)_2(H_2O)_6\}_n$ (**12**)	2D	Triple-stranded layers	Oct.	$CuN_2O_2O_2'$	$\mu\text{-}\eta^1\text{-}\eta^1$; Mono	This work
$\{[Cu_3(\mathbf{4,4'\text{-}bpy})_3(\mu\text{-}OOCH)_4(H_2O)_2](PF_6)_2(H_2O)_6\}_n$ (**13**)[a]	2D	Triple-stranded layers	Oct.	$CuN_2O_2O_2'$	$\mu\text{-}\eta^1\text{-}\eta^1$; Mono	This work
$\{[Cu_3(\mathbf{4,4'\text{-}bpy})_3(\mu\text{-}OOCH)_4(H_2O)_2](BF_4)_2(H_2O)_6\}_n$ (**14**)	2D	Triple-stranded layers	Oct.	$CuN_2O_2O_2'$	$\mu\text{-}\eta^1\text{-}\eta^1$; Mono	This work
$\{[Cu_3(\mathbf{4,4'\text{-}bpy})_3(\mu\text{-}OOCH)_4(H_2O)_2](CF_3SO_3)_2(H_2O)_6\}_n$(**15**) [a]	2D	Triple-stranded layers	Oct.	$CuN_2O_2O_2'$	$\mu\text{-}\eta^1\text{-}\eta^1$; Mono	This work
$\{[Cu(\mathbf{4,4'\text{-}bpy})(\mu\text{-}OOCH)(NO_3)]\}_n$ (**16**)	2D	Zig-zag layers	Oct.	$CuN_2O_2O_2'$	$\mu\text{-}\eta^1\text{-}\eta^2$	This work
$[Cu(OOCH)_2(\mathbf{4,4'\text{-}bpy})]_n$ (**I**)	3D	Framework	Oct.	$CuN_2O_2O_2'$	$\mu\text{-}\eta^1\text{-}\eta^1$	106
Cu(II)/4,4'-bpy/acetato compounds						
$\{[Cu_2(\mathbf{4,4'\text{-}bpy})_2(\mu\text{-}OOCCH_3)_3](ClO_4)(H_2O)\}_n$ (**17**) [a]	2D	Quadruple-stranded layers	Oct. + Int.	CuN_2O_3	$\mu\text{-}\eta^1\text{-}\eta^1$; Mono	This work
$\{[Cu_2(\mathbf{4,4'\text{-}bpy})_2(\mu\text{-}OOCCH_3)_3](PF_6)(H_2O)\}_n$ (**18**)	2D	Quadruple-stranded layers	Oct. + Int	CuN_2O_3	$\mu\text{-}\eta^1\text{-}\eta^1$; Mono	This work
$\{[Cu_2(\mathbf{4,4'\text{-}bpy})_2(\mu\text{-}OOCCH_3)_3](BF_4)(H_2O)\}_n$ (**19**) [a]	2D	Quadruple-stranded layers	Oct. + Int	CuN_2O_3	$\mu\text{-}\eta^1\text{-}\eta^1$; Mono	This work
$\{[Cu_2(\mathbf{4,4'\text{-}bpy})_2(\mu\text{-}OOCCH_3)_3](CF_3SO_3)(H_2O)\}_n$ (**20**) [a]	2D	Quadruple-stranded layers	Oct. + Int	CuN_2O_3	$\mu\text{-}\eta^1\text{-}\eta^1$; Mono	This work
$\{[Cu_2(\mathbf{4,4'\text{-}bpy})(OOCCH_3)(OH)(H_2O)](H_2O)_2(SiF_6)\}_n$ (**II**)	2D	Double-stranded layers	SPy.	CuN_2O_2O'	$\mu\text{-}\eta^1\text{-}\eta^1$	107
$\{[Cu(\mathbf{4,4'\text{-}bpy})(OOCCH_3)_2](H_2O)_{2.5}\}_n$ (**III**)	1D	Double chains	SPy.	CuN_2O_2O'	Mono; Chelate	86
$\{[Cu_2(\mathbf{4,4'\text{-}bpy})_2(\mu\text{-}OOCCH_3)_2(OOCCH_3)_2](H_2O\}_n$ (**IV**)	1D	Double chains	Oct.	$CuN_2O_2O_2'$	$\mu\text{-}\eta^1\text{-}\eta^1$; Chelate	108
$\{[Cu(\mathbf{4,4'\text{-}bpy})(OOCCH_3)_2](H_2O)_3\}_n$ (**V**)	1D	Double chains	SPy.	CuN_2O_2O'	$\mu\text{-}\eta^1\text{-}\eta^1$; Chelate	109
$\{[Cu_2(\mathbf{4,4'\text{-}bpy})(OOCCH_3)_4](CH_3CN)\}_n$ (**VI**)	1D	Polymeric chains	Oct.	$CuN_2O_2O_2'$	$\mu\text{-}\eta^1\text{-}\eta^1$	110
$\{[Cu_2(\mathbf{4,4'\text{-}bpy})(OOCCH_3)_4](DMF)\}_n$ (**VII**)	1D	Polymeric chains	Oct.	CuN_2O_2O'	$\mu\text{-}\eta^1\text{-}\eta^1$	111
Cu(II)/4,4'-bpy/carboxylato compounds						
$[Cu(\mathbf{4,4'\text{-}bpy})(DMIC)_2]_n$ (**VIII**)	1D	Polymeric chains	SP.	CuN_2O_2	Chelate	112
$[Cu(\mathbf{4,4'\text{-}bpy})_{0.5}(ba)_2]_n$ (**IX**)	1D	Polymeric chains	SPy.	CuN_2O_2O'	$\mu\text{-}\eta^1\text{-}\eta^1$	85
$[Cu_2(Hsal)_4(\mathbf{4,4'\text{-}bpy})]_n$ (**X**)	1D	Polymeric chains	Oct.	$CuN_2O_2O_2'$	$\mu\text{-}\eta^1\text{-}\eta^1$	113
$\{$*trans*-$[Cu(Hsal)_2(\mathbf{4,4'\text{-}bpy})](DMF)\}_n$, (**XI**)	1D	Zig-zag chains	Oct.	$CuN_2O_2O_2'$	Chelate	113
$\{$*cis*-$[Cu(Hsal)_2(\mathbf{4,4'\text{-}bpy})](H_2O)_2\}_n$ (**XII**)	1D	Double chains	Oct.	$CuN_2O_2O_2'$	$\mu\text{-}\eta^1\text{-}\eta^1$; Chelate	113

4,4'-bpy = 4,4'-bipyridine; DMIC = 3,5-dimethylisoxazole-4-carboxylate; Hsal = salicylic acid; Hba=benzoic acid. Spy = Square pyramidal; SP = square planar; Int. = Intermediate 5-coordinate geometries; Oct. = distorted octahedral; Mono = Monoatomic-bridged; [a] = propose from spectroscopic properties

4.3 Electronic and EPR spectra

The electronic spectra of triple-stranded 2D layer compounds **12-15** display a broad peak centered at 15.8, 15.5, 15.8 and 15.5 kK and a poorly resolved shoulder at approximately 12.5, 12.3, 12.5 and 12.3 kK, respectively, see Table 2.2 and Figure 4.14. The observed single broad band at ca. 15.8 kK with unresolved shoulder around 12.5 kK, agree with an elongated octahedral geometry with the off-z-axis distortion. The d_{xz}, $d_{yz} \rightarrow d_{x^2-y^2}$ and d_{xy}, $d_{z^2} \rightarrow d_{x^2-y^2}$ transitions[114] may be assigned for the broad band and the low-energy shoulder, respectively. The electronic spectrum of **16** also exhibits a broad peak at 15.2 kK (Figure 4.14) and agrees with a cis-distorted octahedral geometry having an off-z-axis distortion. This observation suggests the assignment of the band as the d_{xz}, d_{yz}, d_{xy}, $d_{x^2-y^2} \rightarrow d_{z^2}$ transition for this compound. The electronic spectra of **17-20**, exhibit a higher energy broad peak centered at 16.5 kK and a poorly resolved shoulder at approximately 12.5 kK (Table 2.2 and Figure 4.14). These spectra are consistent with the mixed stereochemistries: such as an intermediate five-coordinate geometry which usually displays a single broad band at approximately 13.0 kK and the compressed octahedral geometry which usually displays a single broad band at approximately 15.0-16.5 kK and the d_{xz}, d_{yz}, d_{xy}, $d_{x^2-y^2} \rightarrow d_{z^2}$ transitions[114] are tentatively assigned to this single broad band.

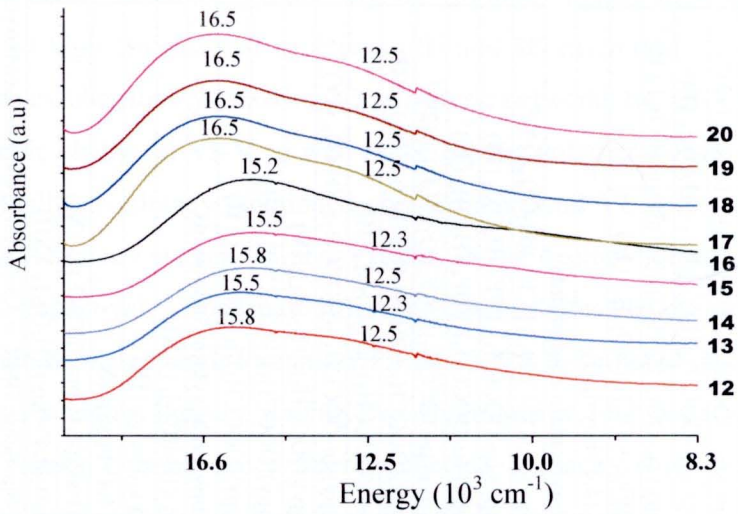

Figure 4.14 The electronic diffuse reflectance spectra of **12-20**

The X-band powder EPR spectra of all compounds have been measured as polycrystalline samples at room temperature and low temperature (70 K) (Figure 4.15 right and left hand, respectively). The Cu(II)-**4,4,'-bpy**-formato compounds (**12-15**) show an axial signal with a $g_{//} = 2.22$ and $g_{\perp} = 2.09$ which is typical for a $d_{x^2-y^2}$ ground state of an elongated octahedral geometry (Figures 4.15A-D). No hyperfine splitting is resolved. The EPR spectrum of **16** exhibits an axial signal with a $g_{\perp} = 2.18$ and $g_{//} = 2.04$ (Figure 4.15E) which is typical for a d_{z^2} ground state of cis-distorted octahedral geometry. This feature is comparable with the EPR spectra of the remaining four Cu(II)-**4,4,'-bpy**-acetato compounds (**17-20**) which also show an axial signal with a $g_{\perp} = 2.22$ and $g_{//} = 2.09$ in agreement with the dominant feature of a compressed octahedral geometry (Figures 4.15F-H), except **20** which shows an axial signal with a $g_{//} = 2.17$ and $g_{\perp} = 2.06$ (Figure 4.15I). This behaviour may probably due to the dominant feature of a five-coordinate environment, distorted towards the square pyramid geometry and/or the octahedral environment distorted towards the elongated octahedral via different H-bonding motifs compared to other compounds. This observation demonstrates that the large trifate anions do have an influence on the CuN_2O_3 or CuN_2O_4 environments.

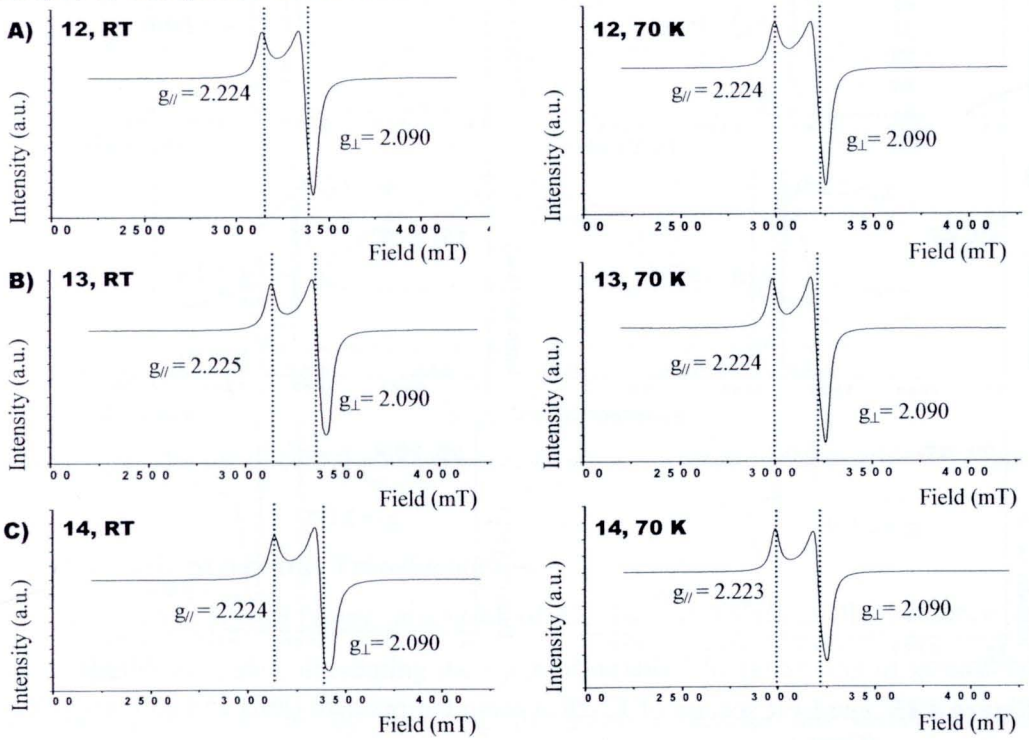

Figure 4.15 The EPR spectra of **12-20** at room temperature (left) and 70 K (right).

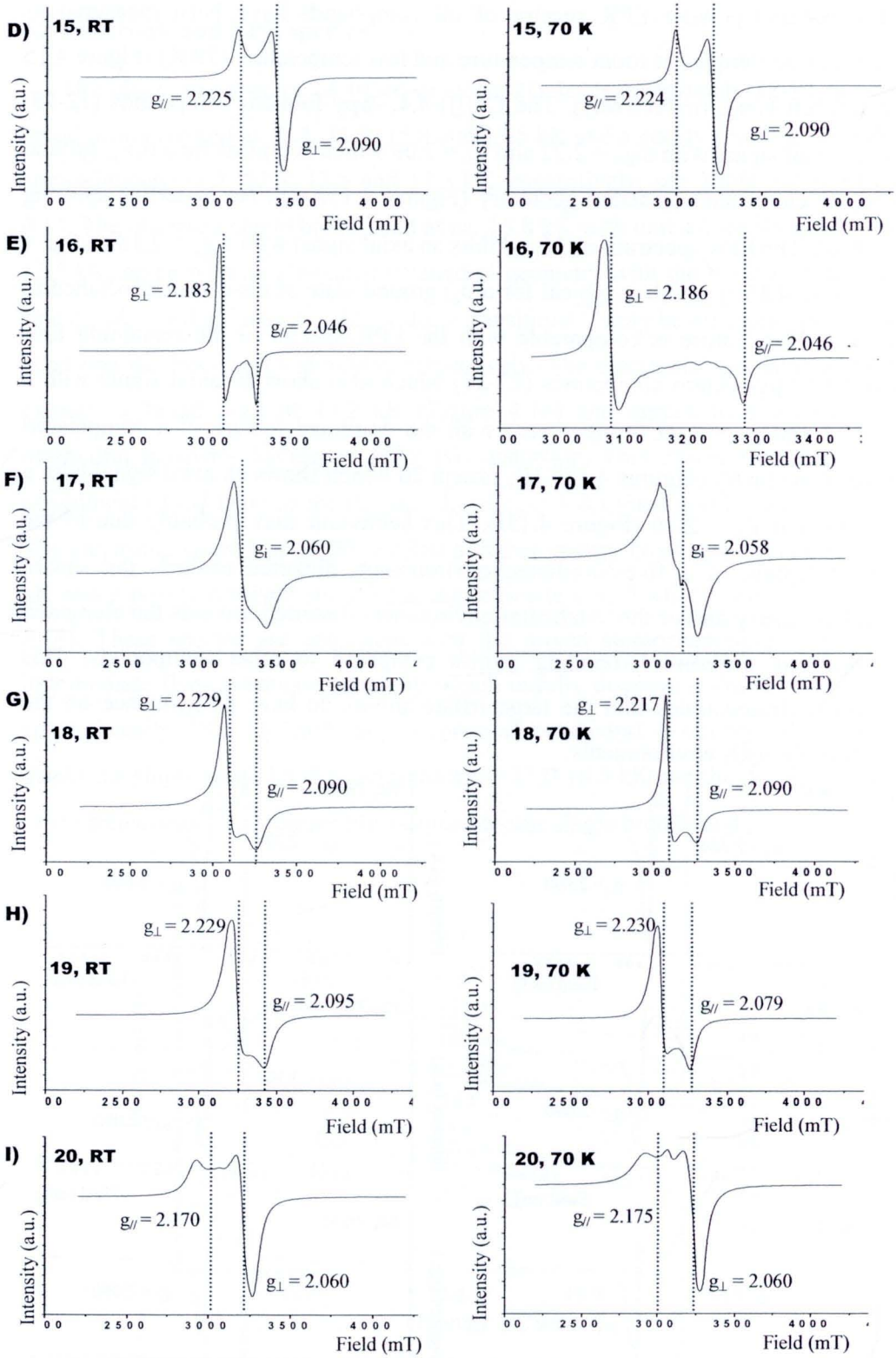

Figure 4.15 The EPR spectra of **12-20** at room temperature (left) and 70 K (right). (Cont.)

4.4 Physical Properties

4.4.1 Thermogravimetric Properties

In order to determine the thermal stability the copper(II)-**4,4,'-bpy**-carboxylato compounds, the thermal decomposition behavior of compounds **12** and **18** was planned to be investigated. Unfortunately, both compounds could not be investigated, as the metal-formate/acetate compounds containing organic ligands are potential explosives; indeed explosions occurres for all copper(II)-**4,4,'-bpy**-carboxylato compounds upon heating at high temperature.

4.4.2 Luminescent Properties

The emission spectra of compounds **12-20** in the solid state at room temperature are shown in Figure 4.16. All compounds display one strong emission, approximately occurring in the range λ_{max} = 420-428 nm ($\lambda_{excitation}$ = 254 nm) and which should be attributed to the charge transfer between the metal and ligand.[90]

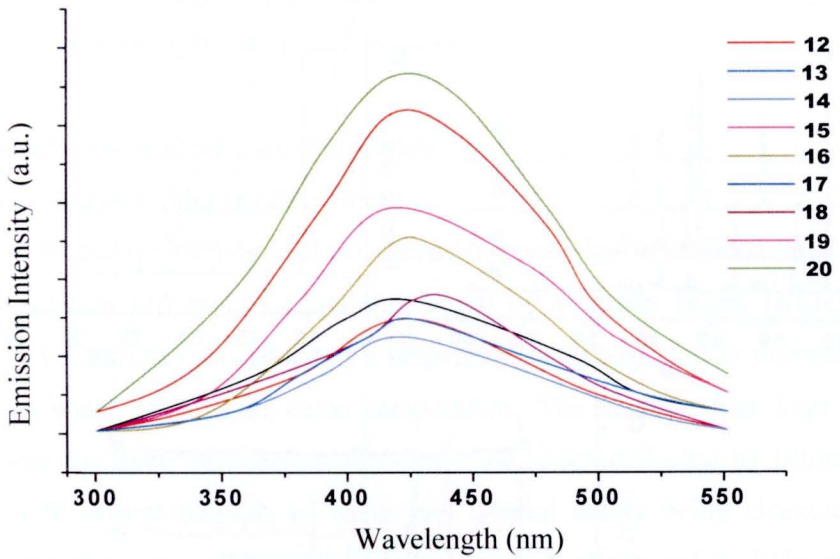

Figure 4.16 The solid-state fluorescent spectra of compounds **12-20** in arbitrary units.

4.5 Dynamic Structural Transformation

The single-crystal X-ray structures of **12**, **14** and **18** reveal the presence of lattice water molecules, illustrating their porous nature. The possibility of generating microporous frameworks by removing the guest molecules has therefore been investigated. Hence, the stability of the different frameworks upon removal/

reintroduction of the guest molecules has been monitored in detail, using elemental analysis and XRPD technique (Table 4.5 and Figure 4.17).

Table 4.5 Elemental analyses of compounds **12**, **14** and **18** and of the products after removal and after reintroduction of the guest water molecules

Compound	Element	Before Removal of water		After Removal of water		After water reintroduction
		Exp. (%)	Cal. (%)	Exp. (%)	Cal. (%)	Exp. (%)
12	C	34.56	34.54	39.21	39.34	39.08
	H	4.18	3.75	2.18	2.72	2.33
	N	7.33	7.11	8.16	8.10	8.16
14	C	34.88	35.30	39.90	40.32	39.17
	H	4.25	3.82	2.36	2.79	2.57
	N	7.28	7.26	8.22	8.30	7.48
18	C	39.76	40.06	40.89	41.01	40.14
	H	3.50	3.49	3.28	3.31	2.23
	N	6.94	7.19	6.98	7.36	6.90

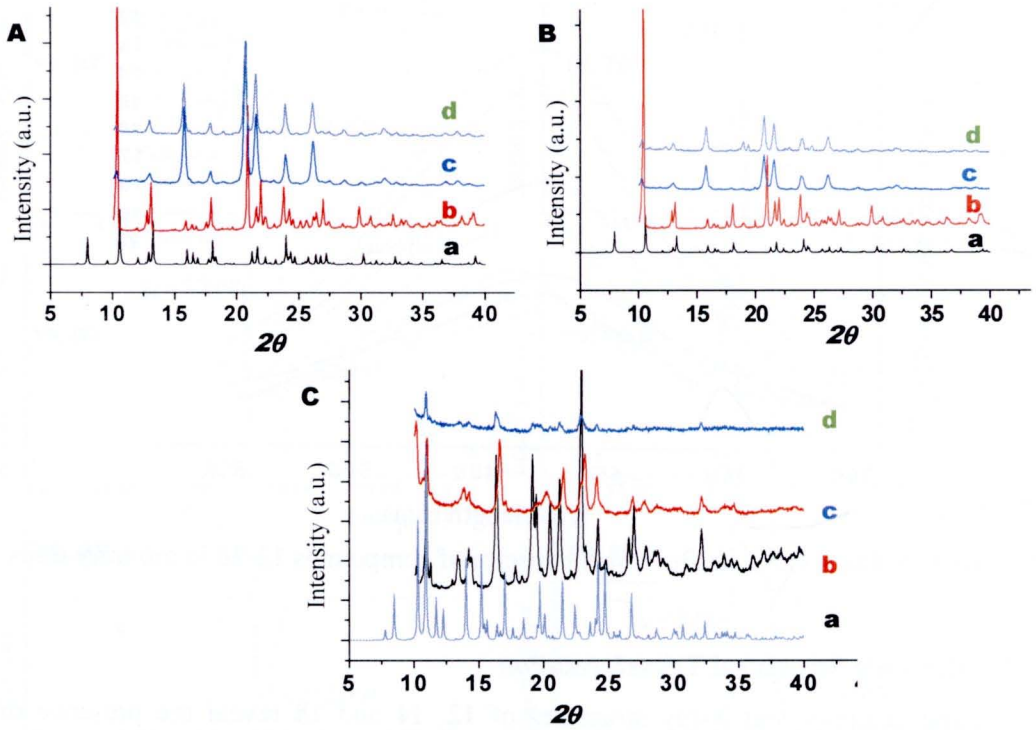

Figure 4.17 A)-C) XRPD patterns of **12**, **14** and **18**, respectively; (a) simulated, (b) as-synthesized, (c) after removal of the guest water molecules, and (d) after reintroduction of the guest water molecules.

The weight loss of three compounds consist of eight water molecules (two coordinated and six lattice water molecules) for **12** and **14**, and one water molecule for **18** when elevating the temperature to 120 °C for 6 h under vacuum. The X-ray powder diffraction reveals the remaining microcrystalline solid with a structure change (Figure 4.17), according to the result of the elemental analysis except for compound **18** which shows that part of crystals has become amorphous (Figure 4.17C). Therefore, the copper(II)-formate/acetate compounds containing **4,4'-bpy** organic ligand are unstable at high temperature. A similar behavior is also observed for Zn(II)-**4,4'-bpy**-formato compounds (**1-5**), as reported in Chapter 3. However, the solid-state structures of all Cu(II) compounds do not collapse when the water molecules are taken out. Unfortunately, the dynamic structural transformation behavior for all Cu(II) compounds cannot be achieved after re-immersing in water. The XRPD after dehydrating is different from the original material, indicating the change in structure, while also the guest water molecules in all compounds cannot be reintroduced after immersing in aqueous solution; the elemental analysis results confirm this feature (Table 4.5).

4.6 Counteranion Exchange Properties

4.6.1 Anion Exchange Procedure

The procedure of a typical counteranion exchange is outlined here first: An aqueous solution (10 mmol) containing a salt of a certain anion, ($KClO_4$, KPF_6, $NaBF_4$, or CF_3SO_3Na) was added to a suspension (1 mmol) of each microcrystalline sample in water (5 mL) at room temperature. The mixture was kept at room temperature for three days before filtration. The solids collected by filtration were washed with several aliquots of water and ethanol before being characterized by infrared spectroscopy, elemental analyses and X-ray powder diffraction. The exchanged species have been compared with those of the corresponding compounds prepared from the direct reaction. The exchanged species were all found to give a sharp X-ray powder diffraction pattern.

4.6.2 Counteranion Exchange

Experimentation aimed at evaluating the ion-exchange properties of this material showed that reversible exchange cannot be achieved. In a typical experiment, the addition of a slight excess of $NaPF_6$ or $NaBF_4$ to a suspension of crystalline **12** in water at room temperature showed that the ClO_4^- anions begin to exchange with PF_6^- and BF_4^- anions after 1 h, as evidenced by X-ray powder diffraction (XRPD), elemental analysis and infrared data. The results are shown in Table 4.6. The IR spectrum of **12** shows an intense ClO_4^- absorption band at 1104-1045 cm^{-1} (Figure 4.18a).[91] However, this absorption band disappears after the complete anion exchange. Instead, a new and intense PF_6^- bands shows up at 846-838 cm^{-1} and for BF_4^- a broad band shows up at 1041-1012 cm^{-1} (Figures 4.18b and c, respectively).[91] Other peaks of the spectrum were found to be only slightly changed. This observation shows that the cavity of the exchanged compound is so flexible that PF_6^- and BF_4^- anions may be incorporated instead of the ClO_4^- anions, without significant structure collapse or decomposition (Scheme 4.1). Unfortunately, the diffraction pattern of **12** significantly changes after the exchange process with a high degree of crystallinity (Figure 4.19A), indicating that the structure does undergo a structural change with the different guest inclusion and has been transformed to a new crystalline product. However, the products still give a sharp X-ray powder diffraction pattern. This pattern is not coinciding with that of the original unexchanged material. The IR spectrum, XRPD pattern and elemental analysis of the exchanged sample (Table 4.6) match that of $\{[Cu_2(\mathbf{4,4'\text{-}bpy})_2(\mu\text{-}OOCCH_3)_3]\ (X)(H_2O_x)\}_n$ when X = PF_6^- (**1-PF$_6$**) and BF_4^- (**1-BF$_4$**), in which the quality of crystals is not good enough for single crystal X-ray analysis. On the other hand, the anions in the remaining compounds **13-15** and **17-20** can be replaced with ClO_4^-, PF_6^- and/or BF_4^- after suspending the crystals of the compound in an aqueous solution of these different anions for three days. The IR spectra show the complete disappearance of the PF_6^- bands at 846-820 cm^{-1} for **13** and **18**, the BF_4^- bands at 1041-1009 cm^{-1} for **14** and **19**, the $CF_3SO_3^-$ bands at 1257-1200 cm^{-1} for **15** and **20**, and the ClO_4^- bands at 1067–1046 cm^{-1} for **17** (Figure 4.18n). Interestingly, all compounds showed anion-exchange with three kinds of anions, the appearance of intense ClO_4^- bands (1117-1050 cm^{-1}) for **13-15** and **18-20** after exchange with ClO_4^- anions (Figure 4.18), the complete appearance of the PF_6^- bands

at 841-838 cm^{-1} for **12**, **14**, **15**, **17**, **19** and **20** after exchange with PF_6^- anions (Figure 4.18) and compounds **12**, **13**, **15**, **17**, **18** and **20** also shows the complete appearance

Scheme 4.1

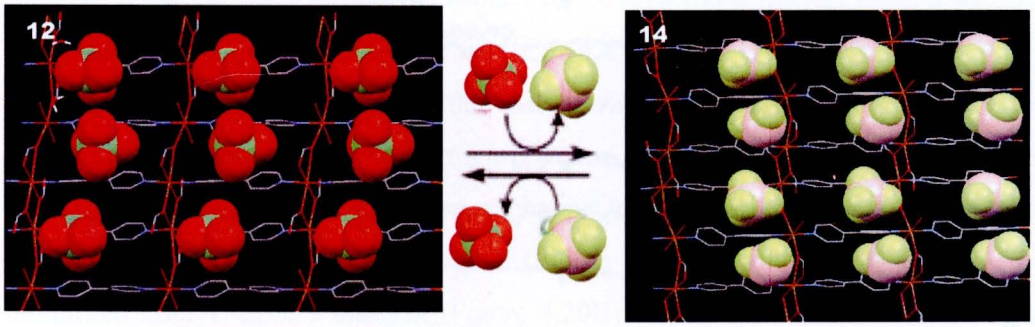

Table 4.6 Elemental analysis of Cu(II)/**4,4'-bpy**/carboxylate compounds and the products obtained from the anion exchange

Compound	Element	Before exchange		After exchange (%)			
		Exp. (%)	Cal. (%)	ClO_4^-	PF_6^-	BF_4^-	$CF_3SO_3^-$
12	C	34.56	34.54		34.45	40.62	
	H	4.18	3.75	-	2.98	3.05	X
	N	7.33	7.11		7.42	8.98	
13	C	31.38	32.07	38.90	-	40.96	
	H	3.87	3.48	3.15		3.43	X
	N	6.61	6.60	9.20		9.84	
14	C	34.88	35.30	38.83	34.54		
	H	4.25	3.82	2.86	3.03	-	X
	N	7.28	7.26	8.79	7.48		
16	C	34.60	33.74	36.89	33.78	39.35	
	H	3.70	3.46	2.49	2.78	2.82	-
	N	7.04	6.56	8.21	7.33	8.42	
17	C	42.40	42.54		35.06	40.58	
	H	3.69	3.71	-	3.82	3.56	X
	N	7.80	7.63		6.94	9.30	
18	C	39.76	40.06	38.22		39.80	
	H	3.50	3.49	3.05	-	3.39	X
	N	6.94	7.19	8.53		8.32	
19	C	42.82	43.29	37.47	35.11		
	H	3.77	3.77	2.93	3.49	-	X
	N	7.44	7.77	8.51	7.01		
20	C	41.22	41.38	37.67	34.85	41.16	
	H	3.59	3.47	2.55	3.37	3.45	-
	N	7.39	7.15	8.09	6.94	8.79	

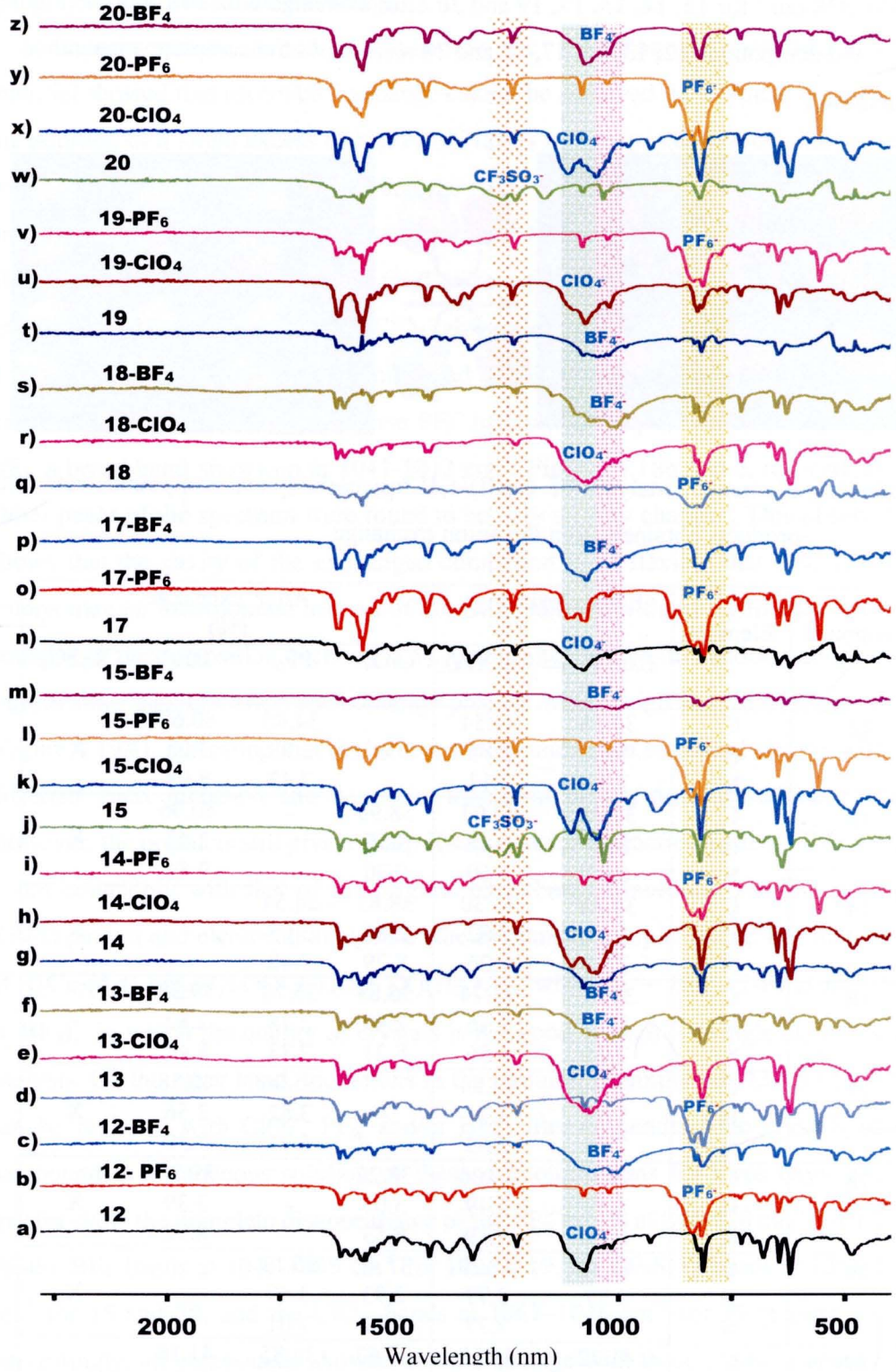

Figure 4.18 IR spectra of (a)-(z) **12-15** and **17-20** as-synthesized and after exchange with $KClO_4$ (**X**-ClO_4), KPF_6 (**X**-PF_6) and $NaBF_4$ (**X**-BF_4).

of the BF_4^- bands at 1041-1012 cm^{-1} after exchange with BF_4^- anions (Figure 4.18). The XRPD patterns of the exchanged species are compared with those of the original compounds prepared from the direct reaction (Figure 4.19). Elemental analysis also supports complete anion exchange (Table 4.6). To investigate the rate of the exchange process, the counteranion exchange of $\{[Cu_2(\mathbf{4,4'\text{-}bpy})_2(\mu\text{-}OOCCH_3)_3](PF_6)(H_2O)\}_n$ (**18**) with ClO_4^- was monitored by the characteristic IR bands of the counteranions under undisturbed condition at room temperature, comparing with the reaction under stirred conditions. The counteranion exchange in water at room temperature was monitored after 2, 10, 20, 40 and 60 h (Figure 4.20A), while the latter case was monitored after 1, 2, 3, 5 and 7 h (Figure 4.20B). The infrared spectrum shows the gradual disappearance of intense PF_6^- peaks (842-838 cm^{-1}) and the appearance and growth of new ClO_4^- peaks (1041-1009 cm^{-1}). The PF_6^- peaks disappear completely already after 4 h by stirring, which is faster than under the undisturbed condition at room temperature which disappear completely after 60 h. The other peaks of the spectrum remain virtually unchanged. This demonstrates that the stirring indeed has an influence on the rate of the anion exchange.

The reverse process of the product, **12-PF_6** which was prepared by anion exchange has also been investigated. The ClO_4^- anions of the original compound **12** was first replaced by the slightly larger PF_6^- anions, giving the product **12-PF_6** (Figure 4.18b). Compound **12-PF_6** was subsequently re-immersed in an excess aqueous ClO_4^- solution. Unfortunately, the original compound **12** was not detectable in the reversible reverse process, even not when crystals of **12-PF_6** were re-immersed in an excess concentrated solution of $NaClO_4$ for three days. Similarly, other products could not be achieved for three days, despite the excess salt concentration. In this case the changing structural motifs of its products are not analogous, which has the different crystal structures and inter-packing as well as inter-conversion of the original compounds. However, the eight coordination polymers is highly selective and the anions in the original compounds can be totally replaced with PF_6^- for **12**, **14**, **15**, **17**, **19** and **20**, ClO_4^- for **13**, **14**, **15** and **18-20**, and BF_4^- for **12**, **13**, **15**, **17**, **18** and **20** (see Scheme 4.2 and Table 4.6).

In summary, these results further highlight the complexities of the self-assembly process and the need to understand the relative importance of the interactions between metal ions and ligands, as well as the anions, during the crystallization process.

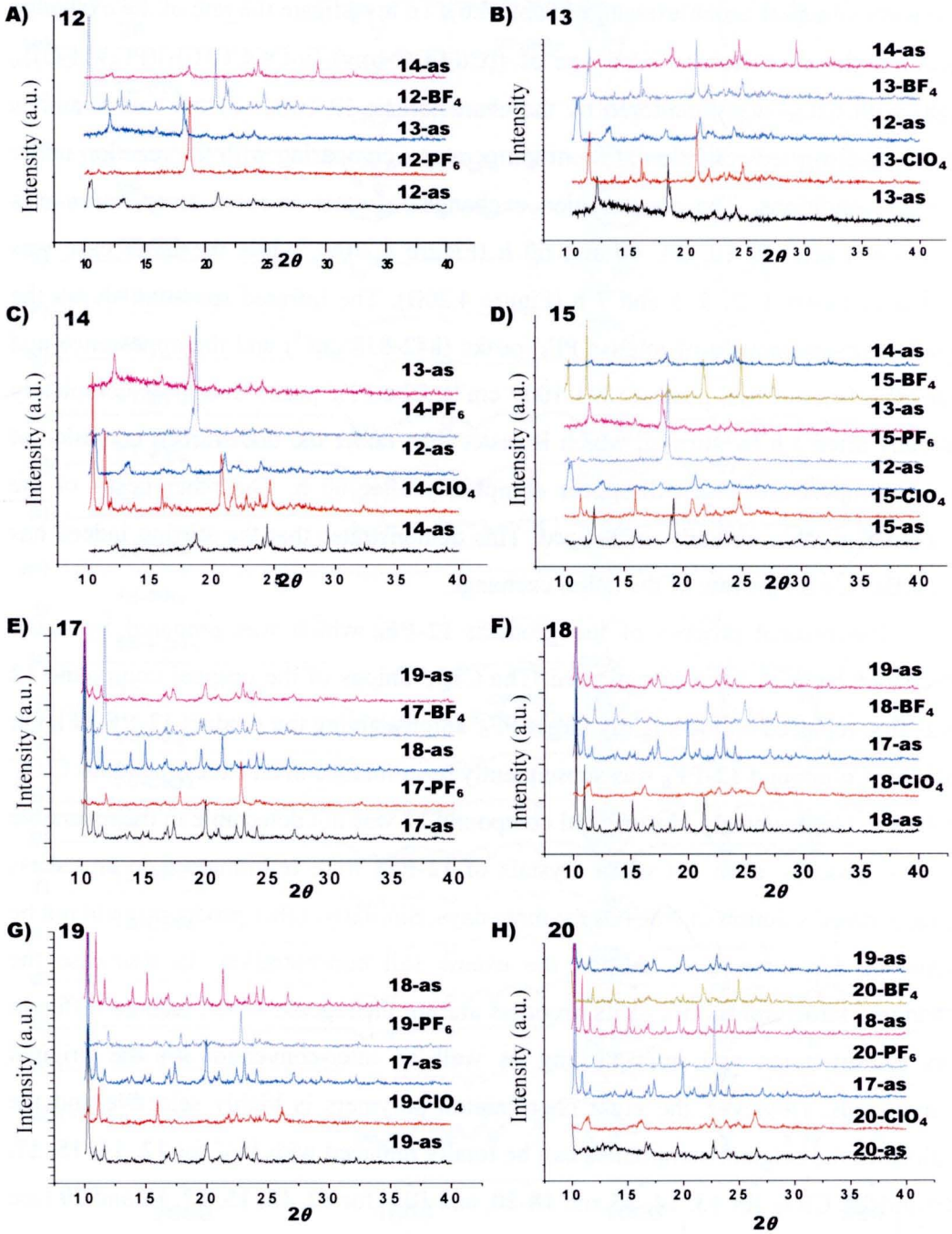

Figure 4.19 (A)-(H) XRPD patterns of **12-15** and **17-20** simulated, as-synthesized, solids obtained after immersing in different solution, solids obtained after re-immersing **X-anion** in an aqueous **anion'** solution (**X-anion'**).

Scheme 4.2 Anion-exchange strategies for compounds **12-15** and **17-20.**

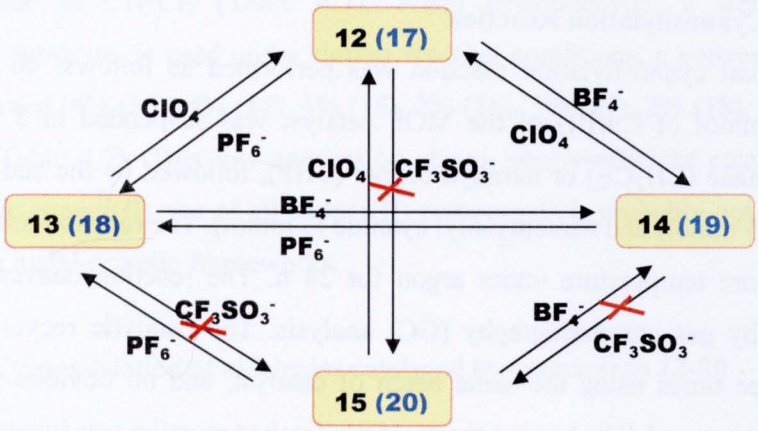

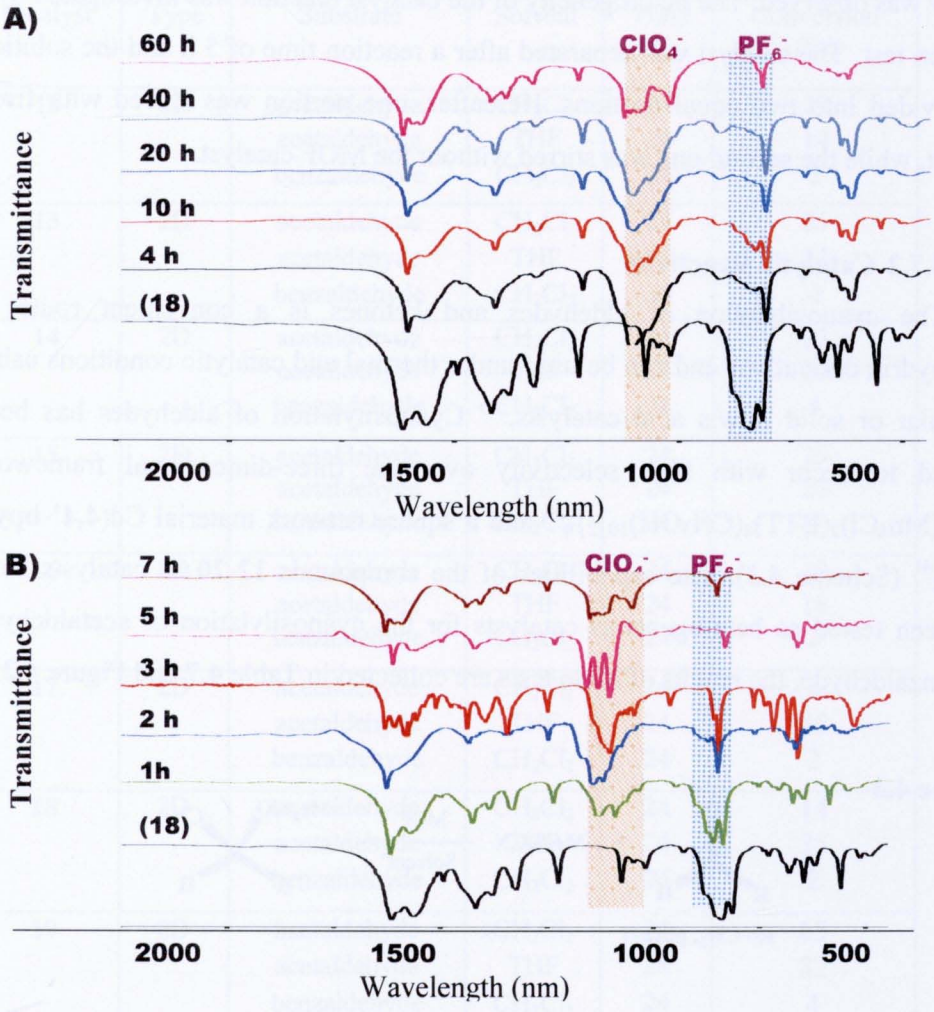

Figure 4.20 IR spectra change procedure during the counteranion exchange of **18** with $KClO_4$ in function of the time on the solid, dried samples at room temperature; A) Undisturbed conditions and B) stirred conditions.

4.7 Catalytic Properties

4.7.1 Cyanosilylation Reaction

A typical cyanosilylation reaction was performed as follows: 40 mg (0.006 mmol, 0.2 mmol of Cu(II)) of the MOF catalyst was suspended in 5 mL of dry dichloromethane (CH_2Cl_2) or tetrahydrofuran (THF), followed by the addition of the aldehyde (1.5 mmol) and trimethylsilyl cyanide (3 mmol). The reaction mixtures were stirred at room temperature under argon for 24 h. The reaction conversions were determined by gas chromatography (GC) analysis. The catalytic recyclability was checked three times using the same batch of catalyst, and no obvious decrease in activity was observed. The heterogeneity of the catalyst reaction was investigated by a filtration test. The catalyst was separated after a reaction time of 5 h and the solution was divided into two equal portions. Hereafter, one portion was stirred with fresh catalyst, while the second one was stirred without the MOF catalyst.

4.7.2 Catalytic Reactivity

The cyanosilylation of aldehydes and ketones is a convenient route to cyanohydrin derivatives and can be used under thermal and catalytic conditions using molecular or solid Lewis acid catalysts.[115] Cyanosilylation of aldehydes has been reported to occur with high selectivity over the three-dimensional framework $\{Mn_3[(Mn_4Cl)_3(BTT)_8(CH_3OH)_{10}]_2\}_n$[55] and a square network material Cd(**4,4'-bpy**)$_2$ $(NO_3)_2$[41] (Scheme 4.3). The capabilities of the compounds **12-20** as catalysts have now been tested as heterogeneous catalysts for the cyanosilylation of acetaldehyde and benzaldehyde, the results of these tests are collected in Table 4.7 and Figure 4.21.

Scheme 4.3

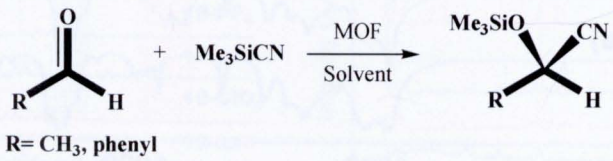

R= CH_3, phenyl

As can be seen, nine of the copper(II)-**4,4'-bpy**-carboxylato compounds are moderately active and selective catalysts for cyanosilylation of aldehydes. The solid **12** is used as catalyst, a conversion of 29% (25% (**13**), 25% (**14**), 25% (**15**), 19% (**16**),

8% (17), 14% (**18**), 65% (**19**) and 14% (**20**)) of acetaldehyde is reached after 24 h reaction time in CH_2Cl_2 (Table 4.7). When benzaldehyde, a sterically more demanding substrate, is used under similar reaction conditions, a conversion of only 2% is observed (4% (**13**), 4% (**14**), 4% (**15**), 2% (**16**), 3% (17), 2% (**18**), 4% (**19**) and 4% (**20**)), Table 4.7). This low conversion shows poorly-efficient catalysts, so the Lewis acidic copper(II) site of all copper(II) compounds is probably not the best test reaction for metal-organic frameworks.

Table 4.7 Cyanosilylation of aldehydes catalyzed by compounds **12-20**

Catalyst	Type	Substrate	Solvent	Time (h)	Conversion (%)
12	2D	acetaldehyde	CH_2Cl_2	24	29
		acetaldehyde	THF	24	14
		benzaldehyde	CH_2Cl_2	24	2
13	2D	acetaldehyde	CH_2Cl_2	24	25
		acetaldehyde	THF	24	23
		benzaldehyde	CH_2Cl_2	24	4
14	2D	acetaldehyde	CH_2Cl_2	24	25
		acetaldehyde	THF	24	27
		benzaldehyde	CH_2Cl_2	24	4
15	2D	acetaldehyde	CH_2Cl_2	24	25
		acetaldehyde	THF	24	20
		benzaldehyde	CH_2Cl_2	24	4
16	2D	acetaldehyde	CH_2Cl_2	24	19
		acetaldehyde	THF	24	16
		benzaldehyde	CH_2Cl_2	24	2
17	2D	acetaldehyde	CH_2Cl_2	24	8
		acetaldehyde	THF	24	45
		benzaldehyde	CH_2Cl_2	24	3
18	2D	acetaldehyde	CH_2Cl_2	24	14
		acetaldehyde	THF	24	35
		benzaldehyde	CH_2Cl_2	24	2
19	2D	acetaldehyde	CH_2Cl_2	24	65
		acetaldehyde	THF	24	82
		benzaldehyde	CH_2Cl_2	24	4
20	2D	acetaldehyde	CH_2Cl_2	24	14
		acetaldehyde	THF	24	71
		benzaldehyde	CH_2Cl_2	24	4

In addition, the conversion of acetaldehyde has been examined for each MOF catalyst immersed in THF. It has been found that the reaction is also less efficient in this solvent, which may be explained by a competitive binding of the substrate and the donor type solvent to the metal site. The 14% yield is achieved after 24 h (23% (**13**), 27% (**14**), 20% (**15**), 16% (**16**), 45% (**17**), 35% (**18**), 82% (**19**), 71% (**20**)), Table 4.7).

It is noted that the catalytic reactivities of compounds **17-20** in THF are higher than other compounds. This might be due to the absence of donating water ligands in their structures. As a result, the copper(II) centers of **17-20** behave as more cationic than the other compounds, and the Lewis acidity increases leading to the more effective binding of the substrate and giving high conversions in THF.[93] The cationic nature and Lewis acidity of the Cu^{2+} center may play a key role and lead to significant differences in the conversion. In addition, the use of THF as solvent for **12-16** is disadvantageous, since it leads to decomposition of the catalyst under this reaction condition, even at room temperature, within days. The decomposition causes a reddish-brown appearance of apparent Cu(I) solid material, with THF as a reducing agent. At room temperature after 24 h the color of the catalyst changes to reddish-brown suggesting full decomposition of the material.

Nevertheless, the catalytic activities of compounds **12-20** for the cyanosilylation of aldehydes have been compared with those of zinc(II) porous coordination frameworks (**1-11**), Table 3.8. The lower catalytic reactivity for **12-20** suggests the Lewis acidicity of copper(II) compounds is lower than zinc(II) compounds resulting the low conversion for this reaction.

4.7.3 Heterogeneity

In order to demonstrate that the reaction mechanism is heterogeneous and not homogeneous, a filter test was carried out. After 5 h (10% conversion reached for **18**), 35% of the THF solution was separated from the catalyst by filtration and the reaction was followed by GC in the remaining suspension containing the solid catalyst, and the filtrate (Figure 4.21). In the filtrate, the reaction does not proceed further, whereas in the catalyst-containing suspension, the conversion of the substrate continues reaching 35% after 24 h (Figure 4.21). Thus, the catalytic activity of **18** most likely originates from the presence of the solid catalyst and is not caused by molecular species that

might have dissolved into solution. Therefore, the filter experiment indicates that the mechanism is heterogeneous and not homogeneous.

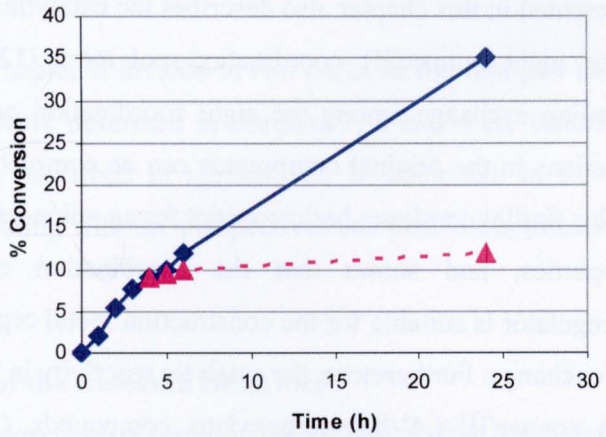

Figure 4.21 Cyanosilylation of acetaldehyde in THF catalyzed by **18** and the effect of filtration of the solid after 4 hrs (purple triangles).

4.8 Conclusions

On the basis of a combination of Cu(II) ion and **4,4'-bpy**, a variety of coordination polymer frameworks were generated by using the carboxylate-regulator anions, namely formato and acetato ligands. The obtained frameworks are the triple-stranded two-dimensional networks $\{[Cu_3(\mathbf{4,4'\text{-}bpy})_2(\mu\text{-}OOCH)_4(H_2O)_2](X)_2(H_2O)_6\}_n$ when X = ClO_4^- (**12**), PF_6^- (**13**), BF_4^- (**14**), $CF_3SO_3^-$ (**15**), the two-dimensional network $\{[Cu(\mathbf{4,4'\text{-}bpy})(\mu\text{-}OOCH)(NO_3)]\}_n$ (**16**) and the quadruple-stranded two-dimensional networks $\{[Cu_2(\mathbf{4,4'\text{-}bpy})_2(\mu\text{-}OOCCH_3)_3](X)(H_2O)\}_n$ when X = ClO_4^- (**17**), PF_6^- (**18**), BF_4^- (**19**), $CF_3SO_3^-$ (**20**). This finding demonstrates that the four anions have hardly any influence on the network formation. The steric effect on the architecture has been investigated by using a slightly different monocarboxylate anion, namely formato and acetato moieties as secondary co-ligands of [Cu(II)/**4,4'-bpy**] coordination units, applying the same reaction conditions. The structures lead to the formation of different structural motifs.

The thermal stability of compounds **12** and **18** and the dynamic structural transformation compounds **12**, **14** and **18** have been investigated. Unfortunately, both compounds are potential explosive at high temperature, as was found for three copper(II)-**4,4,'-bpy**-carboxylato compounds. In addition, the dynamic structural

transformation behavior for all Cu(II)–**4,4-bpy**–carboxylato compounds cannot be achieved after re-immersing in water.

The work presented in this chapter also describes the catalytic reactivity and the anion-exchange for eight copper(II) coordination polymers (**12-15** and **16-20**). Interestingly, the anion exchange among the eight coordination polymers is highly selective and the anions in the original compounds can be completely replaced with different anions. This finding implies a basic concept for an anion-exchange, based on spectroscopic properties, and shows that the combination of **4,4'-bpy** and monocarboxylate-regulator is suitable for the construction metal organic frameworks, followed by anion exchange. Furthermore, the catalytic reactivity in hydrosilylation of the heterogeneous copper(II)-**4,4'-bpy**-carboxylato compounds (**12-20**) has been investigated. It is noted that the catalytic reactivities of compounds **17-20** in THF are higher than those of the other compounds. This difference can be ascribed to the fact that the copper(II) centers of **17-20** have no donating H_2O ligands, and therefor are more cationic than other compounds; so the Lewis acidity increases, leading to more effective binding of the substrate and giving high conversions in THF. The cationic nature and Lewis acidity of the Cu^{2+} center may play a key role and lead to significantly different in the conversion.